JOTCS A
Journal of the Turkish Chemical Society
Section: A
Chemistry
TURKISH CHEMICAL SOCIETY

Evaluation of the Structural, Near-Infrared Luminescence, and Radioluminescence Properties of Nd^{3+} Activated TTB-Lead Metatantalate Phosphors

Mustafa İlhan[1*], İlker Çetin Keskin[2]

[1]Department of Environmental Engineering, Faculty of Engineering, Marmara University, Maltepe, 34840, İstanbul, Turkey
[2]Department of Electricity and Energy, Soma Vocational School, Manisa Celal Bayar University, Soma, 45500, Manisa, Turkey

Abstract: The study reports the structural and spectroscopic properties of Nd^{3+} doped lead metatantalate phosphor series fabricated by conventional solid state method. XRD results of the $PbTa_2O_6$ phase confirm the tungsten bronze symmetry and single-phase structure between 0.5 and 10 mol% Nd^{3+} concentrations. The lead decrease in the structure can be associated with maintaining the charge balance and single phase due to evaporation during sintering. In SEM micrographs, the grains exhibited shapeless morphology, and the grain sizes varied from 0.5 to 7 μm. In EDS results, the increase of Ta/Pb ratio in grain surfaces indicated some lead evaporation, as reported in previous studies. The absorption spectrum of $PbTa_2O_6$ host peaked around 275-280 nm, and the band gap was found to be 3.7±0.2 eV. The absorptions of Nd^{3+} doped phophors shifted the high wavelenght or the low band gap, where the band gaps were found between 3.1±0.2 and 3.3±0.2 eV. The PL emissions of the phosphors in near-inrared region were observed with the transitions of $^4F_{3/2}\rightarrow{}^4I_{9/2}$ (at 875 nm) and $^4F_{3/2}\rightarrow{}^4I_{11/2}$ (at 1060 nm) of Nd^{3+}. The RL emissions or X-ray excited luminescence were monitored with the transitions of $^4F_{3/2}\rightarrow{}^4I_{9/2}$ (at 875 nm), $^4F_{3/2}\rightarrow{}^4I_{11/2}$ (at 1065 nm) in the infrared region, and the transitions of $^2F(2)_{5/2}\rightarrow{}^4F_{9/2}$, $^2F(2)_{5/2}\rightarrow{}^2H(2)_{11/2}$, $^2F(2)_{5/2}\rightarrow{}^4G_{5/2}$, $^2F(2)_{5/2}\rightarrow{}^4G_{7/2}$, $^2F(2)_{5/2}\rightarrow{}^4G_{9/2}$ in the visible region corresponding to at around 430, 455, 490, 525, and 570 nm, respectively. PL and RL emissions of the phosphors exhibited the decreasing emission intensity over 5 mol% due to the concentration quenching which may be associated with cross-relaxing mechanism. In the PL and RL spectral profiles, the similarity of splitting levels was attributed to the similarity of the local symmetry of the ligand ions surrounding the Nd^{3+} ion. The CIE coordinates obtained using RL emissions were found close to the blue region due to visible region transitions.

Keywords $PbTa_2O_6$, Near infrared luminescence, Radioluminescence, Nd^{3+}

Submitted: December 09, 2022. **Accepted:** March 22, 2023.

Cite this: Ilhan M, Keskin IC. Evaluation of the Structural, Near-Infrared Luminescence, and Radioluminescence Properties of Nd3+ Activated TTB-Lead Metatantalate Phosphors. JOTCSA. 2023;10(2):453–66.

DOI: https://doi.org/10.18596/jotcsa.1216564.

***Corresponding author. E-mail:** mustafa.ilhan@marmara.edu.tr.

1. INTRODUCTION

Rare earth (RE) ions with 4f– 4f inner shell transitions have undoubtedly contributed greatly to the development of luminescence applications and the increase in their usage areas. Therefore, the RE ion activated phosphors lead to numerous innovations in the development of new generation devices in various fields such as screen-display technology, lighting technology, and optical data communication due to some positive features such as long life, energy saving, improved physical durability, small size, fast switching, high efficiency, and environmental friendliness (1-19). The trivalent neodymium ion (Nd^{3+}), one of the oldest trivalent lanthanide ions used in solid-state laser, is well known for its useful laser transitions such as

$^4F_{3/2}\rightarrow{}^4I_{9/2}$, $^4F_{3/2}\rightarrow{}^4I_{11/2}$, and $^4F_{3/2}\rightarrow{}^4I_{13/2}$ (20-29). The $^4F_{3/2}\rightarrow{}^4I_{9/2}$ transition at 880 nm finds application as a powerful diode laser transition while the $^4F_{3/2}\rightarrow{}^4I_{11/2}$ transition stands out due to its easily operated at room temperature and pumped efficiently by flash lamp (29). The scintillator or radioluminescent materials convert the high-energy ionizing radiation of a photon into visible-ultraviolet low energy photon. In radioluminescence process, when the energy absorbed in the host material is induced by high-energy radiation, then the energy passes to the RE emission center and the photons are emitted in a relaxation process. The radioluminescent or scintillator materials are used such as in the high energy or nuclear physics detectors, the advanced techniques for homeland security, the high-tech industrial applications, and the medical imaging techniques (to detect accelerated particles and high-energy photons) (30–36).

There are two polymorphs of $PbTa_2O_6$ formed in the PbO-Ta_2O_5 binary system. The high-temperature polymorph is orthorhombic, and the low-temperature polymorph is rhombohedral. The non-ferroelectric rhombohedral is persistent only below around 1150 °C, while the ferroelectric orthorhombic forms at high temperatures (over 1150 °C), and the Curie point is 265 °C (37,38). The orthorhombic $PbTa_2O_6$ shows close structural similarity with the tungsten bronzes in paraelectric state. Tetragonal tungsten bronze (TTB) based oxide structures, which stand out with their dielectric properties, form a wide family of crystals (39-42). TTB structures exhibit suitable host features for dopant lanthanide ions due to its three different tunnels or multi-location sites that allow cation substitution at different radius and charge (30–32). In the literature, there are some studies on $PbTa_2O_6$ due to its structural, dielectric, ferroelectric (37-39), luminescence (30–32), and photocatalytic properties (43).

In the study, the near infrared photoluminescence and radioluminescence properties of $PbTa_2O_6$:xNd^{3+} (x=0.5, 1.5, 3, 5, 7, 10 mol%) phosphors were studied. Although Eu^{3+} (30,40) and Dy^{3+} (31,32) doped studies of the lead tantalate phophors have been reported previously, the Nd^{3+} doped photoluminescence and X-ray excited luminescence are reported in this study to the best of our knowledge. The spectroscopic and structural characterizations of the ceramic samples were examined by XRD, SEM-EDS, PL, RL and absorption analyses.

2. EXPERIMENTAL SECTION

Undoped and $PbTa_2O_6$:xNd^{3+} (x=0.5, 1.5, 3, 5, 7 and 10 mol%) materials were fabricated by the solid state reaction route. $Pb(NO_3)_2$, Ta_2O_5 and Nd_2O_3 powders were used as starting and dopant materials with purity of 99% (Sigma–Aldrich), 99.9% (Alfa Aesar), and 99.9% (Alfa Aesar), respectively. Ta_2O_5 and $Pb(NO_3)_2$ powders were weighed and mixed according to $PbTa_2O_6$ stoichiometry. Six different powder mixtures were prepared and Nd_2O_3 dopant was subsequently added at different concentrations into the each powder mixture as $PbTa_2O_6$:0.005Nd^{3+}, $PbTa_2O_6$:0.015Nd^{3+}, $PbTa_2O_6$:0.03Nd^{3+}, $PbTa_2O_6$:0.05Nd^{3+}, $PbTa_2O_6$:0.07Nd^{3+}, $PbTa_2O_6$:0.1Nd^{3+}, and they were homogenized by mixing in agate mortar for 10 min. Final powder mixtures were heat treated at 1250 °C for 6 h in an electric furnace under air atmosphere after pelleting.

The phase structure of the ceramics was investigated by X-ray diffraction (D2 PHASER, Bruker Corp., Germany) using Cu-K_α radiation, Ni filter, scan rate = 2 °/min, 2θ=20-65°. The grain morphology and elemental identification of the samples were carried out by SEM (JSM-5910LV, JEOL Ltd., Japan) equipped with EDS (INCAx-Sight 7274, Oxford Industries, UK) after Au coating. The near emission spectra of Nd^{3+} doped samples were taken using a diode laser of 800 nm at 300 K. The radioluminescence spectra of the Nd^{3+} doped $PbTa_2O_6$ phosphors were taken using a Machlett OEG-50A tube which operates with 30 kV and 15 mA and, the X-ray tube provides white X-rays at a dose rate of 30 Gy/min radioluminescence spectra were taken with a Horiba Jobin Yvon spectrometer connected to a liquid nitrogen-cooled CCD detector. RL analysis was performed under room conditions, the detector integration time was set to 5 seconds and the input-output slit widths were set to 2 mm. The absorption spectra of the undoped sample and Nd^{3+} doped samples were performed by a Perkin-Elmer Lambda spectrophotometer (USA).

3. RESULTS AND DISCUSSION

3.1. XRD and SEM-EDS Results

The XRD results of undoped sample and $PbTa_2O_6$:xNd^{3+} (x=0.5, 1.5, 5, 7 and 10 mol%) samples are shown in Figure 1. As seen in the XRD patterns of all the samples, there are no different minor phases in the range of 20°-65°. XRD analysis showed that the $PbTa_2O_6$ samples crystallized (JCPDS card No. 14–0315) in the tetragonal tungsten bronze symmetry with space group *P4/mbm*. The orthorhombic-tetragonal relationship of $PbTa_2O_6$ along the c-axis in the tungsten bronze structure is shown in Figure 2. The lattice parameters of tetragonal are a=12.49 Å, c=3.875 Å (37), while the cell data for orthorhombic are a_0=17.68 Å, b_0=17.72 Å, c_0=7.754 Å (38). The relation of the orthorhombic–tetragonal cell parameters is $a_0=a\sqrt{2}$, $b_0=a\sqrt{2}$, $c_0=2c$ (38,44), The a, and b constants are nearly equal, where the b/a ratio is about 1.002 (38). So, the XRD patterns of orthorhombic $PbTa_2O_6$ may be indexed quite well as tetragonal due to the extremely small orthorhombic distortion (38,41). The $A_4B_2C_4M_{10}O_{30}$ formula represents the TTB (tetragonal tungsten bronze) structure for the oxide compounds where the pentagonal (A), square (B), triangle (C) sites have 15, 12, 9 CN, respectively,

and the octahedral (M) sites have 6 CN. The A and B sites are occupied by large cations while the C sites occupied by small cations such as Li^{+}. The M octahedral sites are suitable for small radius and high charged cations such as Ta^{5+}, Nb^{5+}. Li et al. (45) studied the distribution of Eu^{3+} atoms in the A (non-centrosymmetric) sites and B (centrosymmetric) sites, which are related to $^{5}D_{0}\rightarrow{}^{7}F_{2}$, and $^{5}D_{0}\rightarrow{}^{7}F_{1}$ transitions, respectively. They suggested that Eu^{3+} atoms could mainly occupy the centrosymmetric sites or then randomly disperse into both centrosymmetric and non-centrosymmetric sites. Accordingly, based on the ionic radius and coordination number (CN), the formation of the single-phase may be attributed to the partial occupation of vacant sites in the lattice by Nd^{3+} ions (1.27 Å for 12 CN, and 1.163 Å for 9 CN), and partial substitution of Nd^{3+} ions by Pb^{2+} ions (1.35 Å for CN 9, and 1.49 Å for CN 12). In addition, although the inclusion of Nd^{3+} ions does not cause any change in the single-phase structure of $PbTa_2O_6$ up to 10 mol %, the charge balance of structure may be somewhat affected. However, during sintering, a lead decrease may occur due to evaporation, which can be helpful in maintaining the charge balance and single-phase structure in the case of RE doping (40,41).

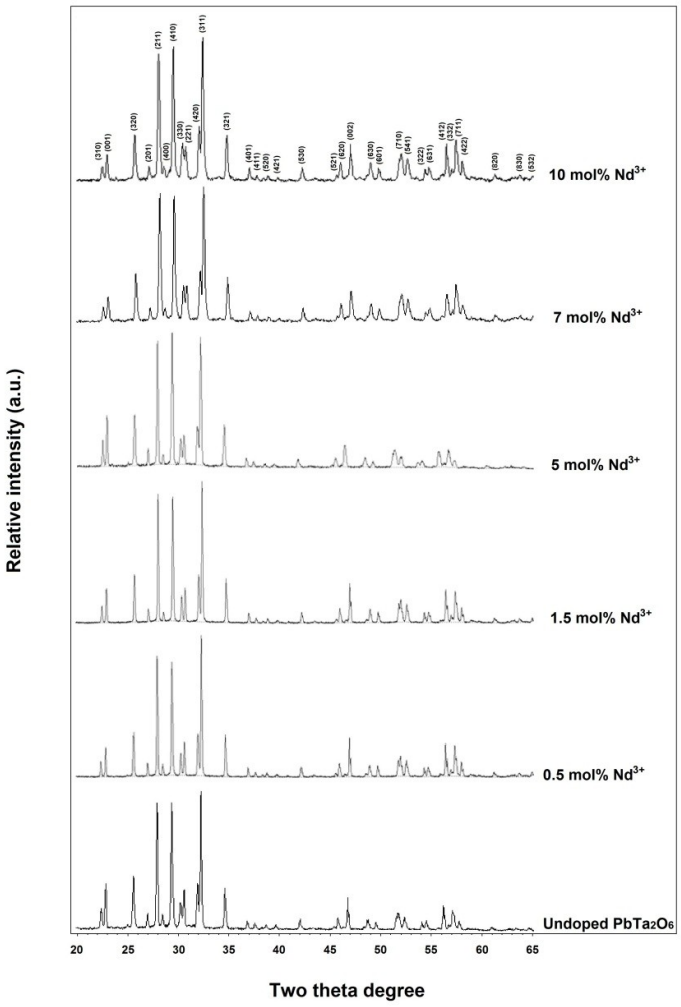

Figure 1: XRD results of undoped, and 0.5, 1.5, 5, 7, 10 mol% Nd^{3+} doped samples.

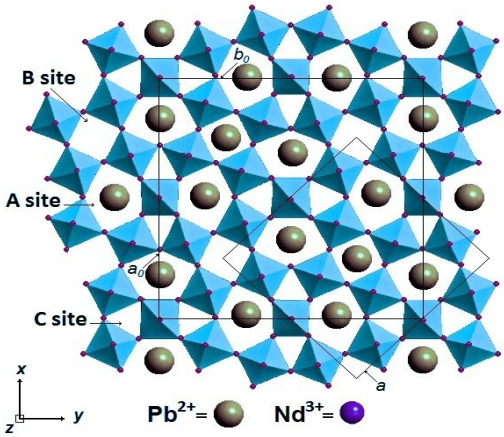

Figure 2: Schematic illustration of the orthorhombic-tetragonal relationship of $PbTa_2O_6$ crystal in the direction of the c axis.

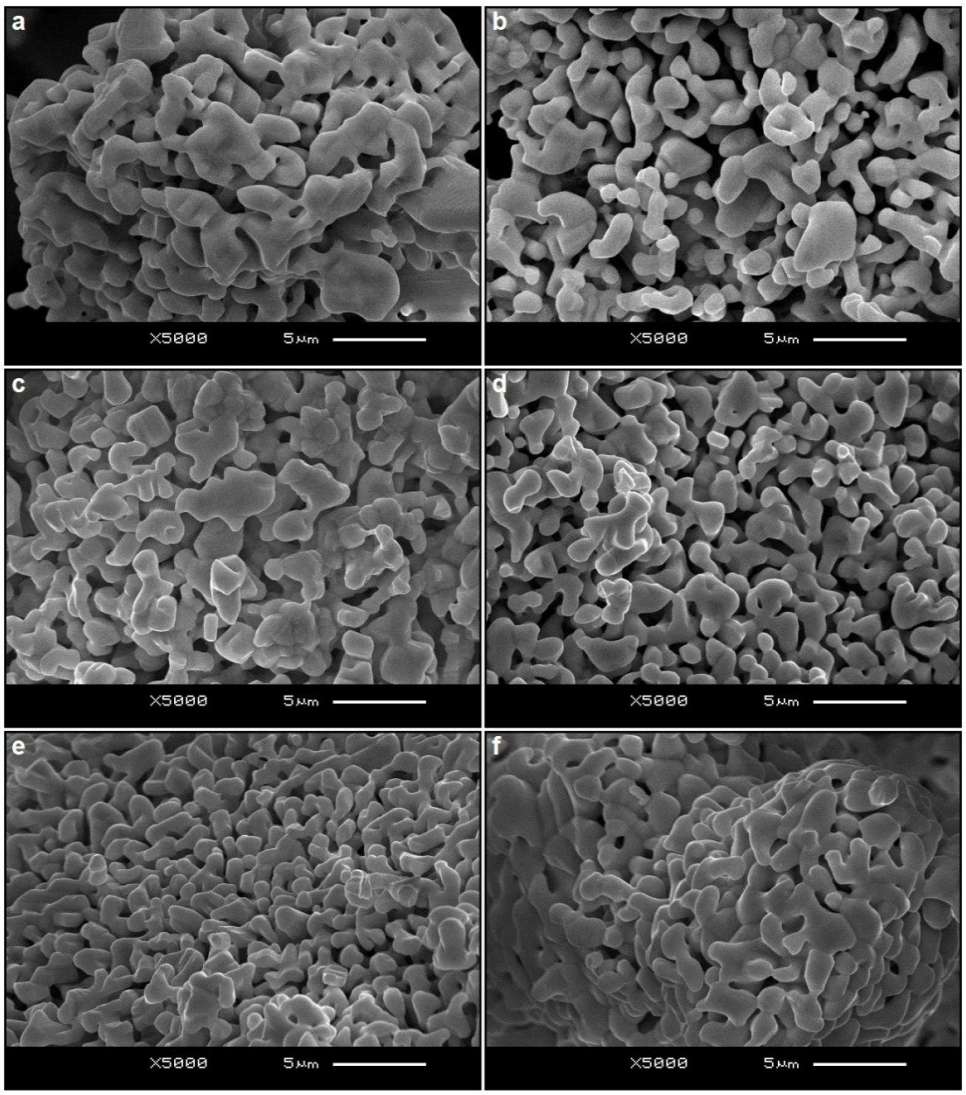

Figure 3: SEM micrographs of (a) undoped and (b) 0.5, (c) 1.5, (d) 5, (e) 7 (f) 10 mol% Nd^{3+} doped samples at 5000× magnifications.

Figure 3(a-f) shows the SEM micrographs at 5.000x magnification for undoped and 0.5, 1.5, 5, 7 and 10 mol% Nd^{3+} doped samples, respectively. The grain shapes of Nd^{3+} doped samples have oval, expanded and a shapeless morphology, while the grain sizes varied from 0.5 to 7 μm. Figure 4 shows the EDS spectrum and elemental compositions as "weight (%) and atomic (%)" for 7 mol% Nd^{3+} doped $PbTa_2O_6$ sample were detected by EDS at 20 kV of SEM acceleration voltage. According to the EDS results, the atomic theoretical (%) composition of Ta grains is 21.74, while the atomic (%) composition of lead is 8.17. The high Ta/Pb ratio indicates a decrease in the amount of Pb due to some evaporation, as reported in previous studies (40,41).

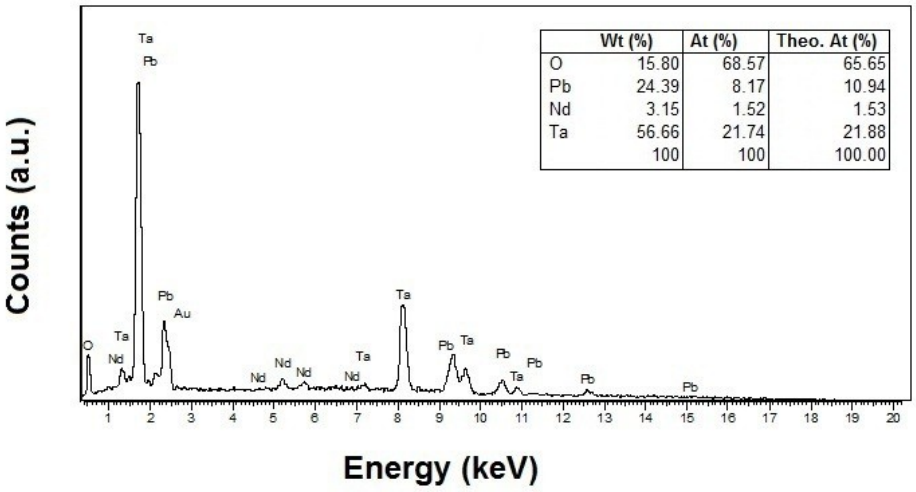

	Wt (%)	At (%)	Theo. At (%)
O	15.80	68.57	65.65
Pb	24.39	8.17	10.94
Nd	3.15	1.52	1.53
Ta	56.66	21.74	21.88
	100	100	100.00

Figure 4: EDS spectrum and wt%, at% elemental compositions, and theoretical at% values for 7 mol% Nd^{3+} doped sample

3.2. Near infrared photoluminescence of Nd^{3+} doped $PbTa_2O_6$ phosphors

Figure 5(a,b) shows the absorption spectra and the band gaps for undoped $PbTa_2O_6$ and 1.5, 5, 10 mol% Nd^{3+} doped phosphors. In Figure 5a, the absorption spectrum of undoped $PbTa_2O_6$ reached the peak value around 275-280 nm, and the band gap was estimated to be 3.7±0.2 eV. Tauc Plot method [46] was used to determine optical band gaps utilizing absorption spectra of undoped $PbTa_2O_6$ and Nd^{3+} doped phosphors. In the literature, the energy gap of $PbTa_2O_6$ is reported by some researchers as 3.7 eV (43) and 3.6-3.9 eV (47), which are consistent with the energy gap found in the study. The optical absorption of phosphors affected by Nd^{3+} concentration and shifted to visible region. In Figure 5b, the optical band gap of $PbTa_2O_6$ host exhibited a decrease with Nd^{3+} concentration. The band gaps of the phosphors were found as 3.3±0.2, 3.2±0.2, and 3.1±0.2 eV for 1.5, 5, and 10 mol% Nd^{3+} concentrations, respectively. The RE^{3+} ion doping can cause increased structural defects in the host lattice and localized states in the band gap, which decreases the energy band gap (48-50). The change in the optical band gap can be explained by the Burstein-Moss phenomenon (51). Accordingly, the dopant ions can cause the formation of subbands in the available band gap, so that the improvement in the conduction property, which becomes continuous depending on the density in the subbands, and eventual merger with the conduction band can occur.

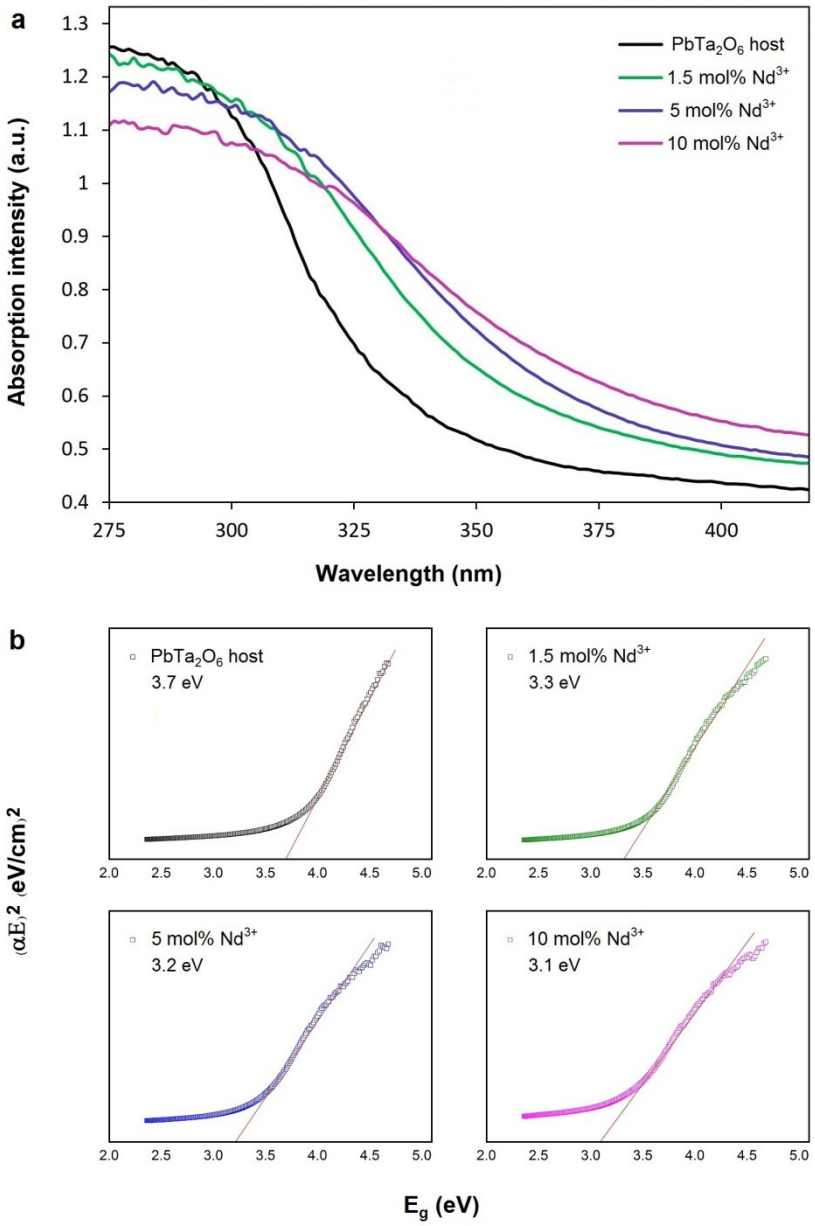

Figure 5: The absorption spectra (a) and the band gaps (b) for the $PbTa_2O_6$ host and $PbTa_2O_6$:xNd^{3+} (x=1.5, 5, 10 mol%) phosphors.

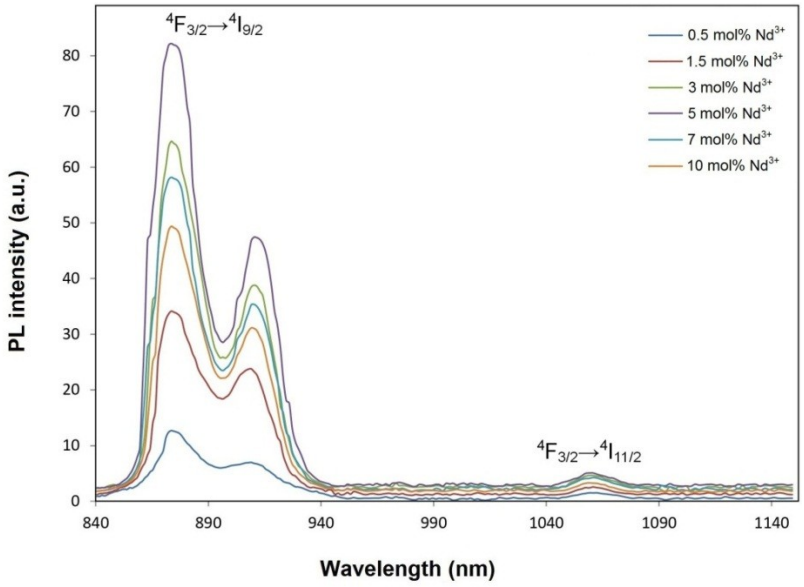

Figure 6: NIR photoluminescence of $PbTa_2O_6$:xNd^{3+} (x=0.5, 1.5, 3, 5, 7, 10 mol%) phosphors by diode laser under 800 nm excitation.

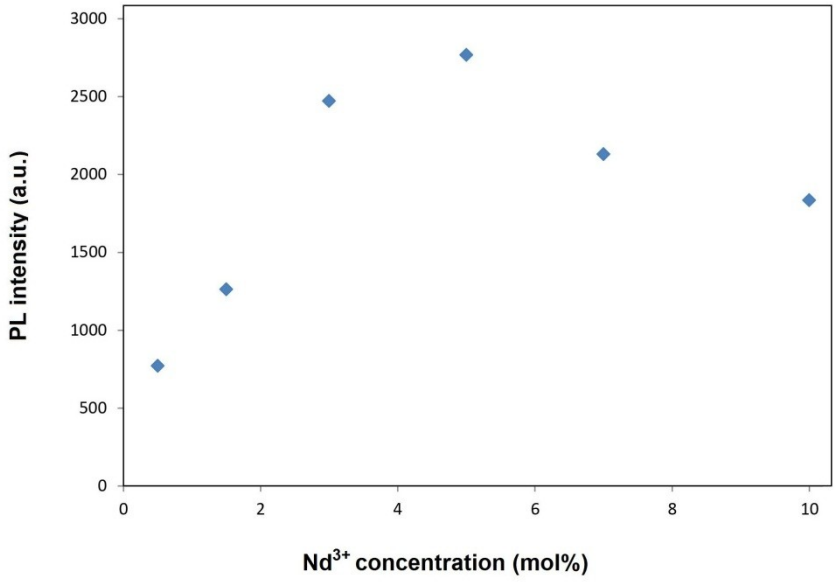

Figure 7: NIR photoluminescence variation of Nd^{3+} doped $PbTa_2O_6$ phosphors depending on doping concentration.

The NIR photoluminescence spectra of $PbTa_2O_6$:xNd^{3+} (x=0.5, 1.5, 3, 5, 7, 10 mol%) phosphors under the excitation of 800 nm using a laser diode are shown in Figure 6. The NIR emissions were recorded corresponding to the $^4F_{3/2}\rightarrow{}^4I_{9/2}$ and $^4F_{3/2}\rightarrow{}^4I_{11/2}$ transitions at 875 and 1060, respectively. The $^4F_{3/2}\rightarrow{}^4I_{9/2}$ transition (at 875 nm) is a potential laser transition that appears to be more intense than the $^4F_{3/2}\rightarrow{}^4I_{11/2}$. Figure 7 shows the change of NIR emissions of $PbTa_2O_6$:Nd^{3+} phosphors depending on doping concentration. As seen in Figure 7, the NIR emission of the phosphor increased up to 5 mol %, and then decreased at 7 and 10 mol% due to the concentration quenching effect. An increase in Nd^{3+} concentration will lead to a shortening of the distance between Nd^{3+}-Nd^{3+}, where the cross-relaxation mechanism is increasingly important (21,32). Thus, the decreasing distance between Nd^{3+} ions will make the cross-relaxation mechanism more effective over 5 mol% Nd^{3+} concentration, and the probability of non-radiative transitions will be higher. The critical distance (R_c) for concentration

quenching will be important, as the decreasing distance of Nd^{3+} ions will promote non-radiative energy transfer. The Blasse's equation (1) estimates the energy transfer between Nd^{3+}-Nd^{3+} ions (52):

$$R_c \approx 2\left(\frac{3V}{4\pi X_c N}\right)^{\frac{1}{3}} \quad \text{(Eq. 1)}$$

Where V is the unit cell volume, N is the number of available sites for dopant ion, X_c is the critical concentration of dopant ion. For $PbTa_2O_6$:Nd^{3+} phosphor, it is X_c =0.10 mol ion in the unit cell (for 0.05 mol), V=604.5 Å^3 (37), and N=5 (6). The critical distance (R_c) between Nd^{3+}–Nd^{3+} ions for energy transfer was calculated as 13.22 Å. Based on Blasse's theory (53), since the Nd^{3+}–Nd^{3+} distance is larger than 5 Å, the effective mechanism will be the multipolar interaction or the mechanism of exchange interaction will ineffective.

3.3. Radioluminescence of Nd^{3+} doped $PbTa_2O_6$ phosphors

Figure 8(a,b) shows the near-infrared and visible region RL emissions under X-ray excitation of $PbTa_2O_6$:xNd^{3+} (x=0.5, 1.5, 3, 5, 7, 10 mol%) phosphors. In Figure 8a, the strong NIR emissions peak about at 875 nm arise from the $^4F_{3/2}\rightarrow{}^4I_{9/2}$ transition, where the splits are observed in the range of 840–950 nm. Also, the weak emission peak is seen around 1065 nm corresponding to the $^4F_{3/2}\rightarrow{}^4I_{11/2}$ transition. The near-infrared emission of the X-ray-excited mechanism exhibited a decrease at 7 and 10 mol% concentrations, similar to PL. As well known for Nd^{3+}, each energy level can be subdivided into 2J+1 sublevels by the local crystal field around the Nd^{3+} ions, but the overall energy level structure of the Nd^{3+} ion does not change greatly in different hosts, because the 4f electrons are shielded by the outer shell $5s^2$ and $5p^6$ electrons (54). On the other hand, impurities such as a secondary phase can cause differences in splitting levels or Stark components where the local symmetry of the ligand ions differs (22-24). As seen from the RL emission spectra in Figure 8a, the $^4F_{3/2}\rightarrow{}^4I_{9/2}$ manifold of Nd^{3+} ions are splitted due to the symmetry of the $PbTa_2O_6$ cation sites, and the splitting levels are similar in the spectral profile. This phenomena may be attributed to the similarity of local symmetry of ligand ions surrounding the Nd^{3+} ion (28). The weak visible RL emissions of the phosphors between 400-600 nm are seen in Figure 8b. The RL emission bands originated from 4f-4f transitions of Nd^{3+} about at 430, 455, 490, 525, and 570 nm correspond to the transitions of the $^2F(2)_{5/2}\rightarrow{}^4F_{9/2}$, $^2F(2)_{5/2}\rightarrow{}^2H(2)_{11/2}$, $^2F(2)_{5/2}\rightarrow{}^4G_{5/2}$, $^2F(2)_{5/2}\rightarrow{}^4G_{7/2}$, and $^2F(2)_{5/2}\rightarrow{}^4G_{9/2}$, respectively.

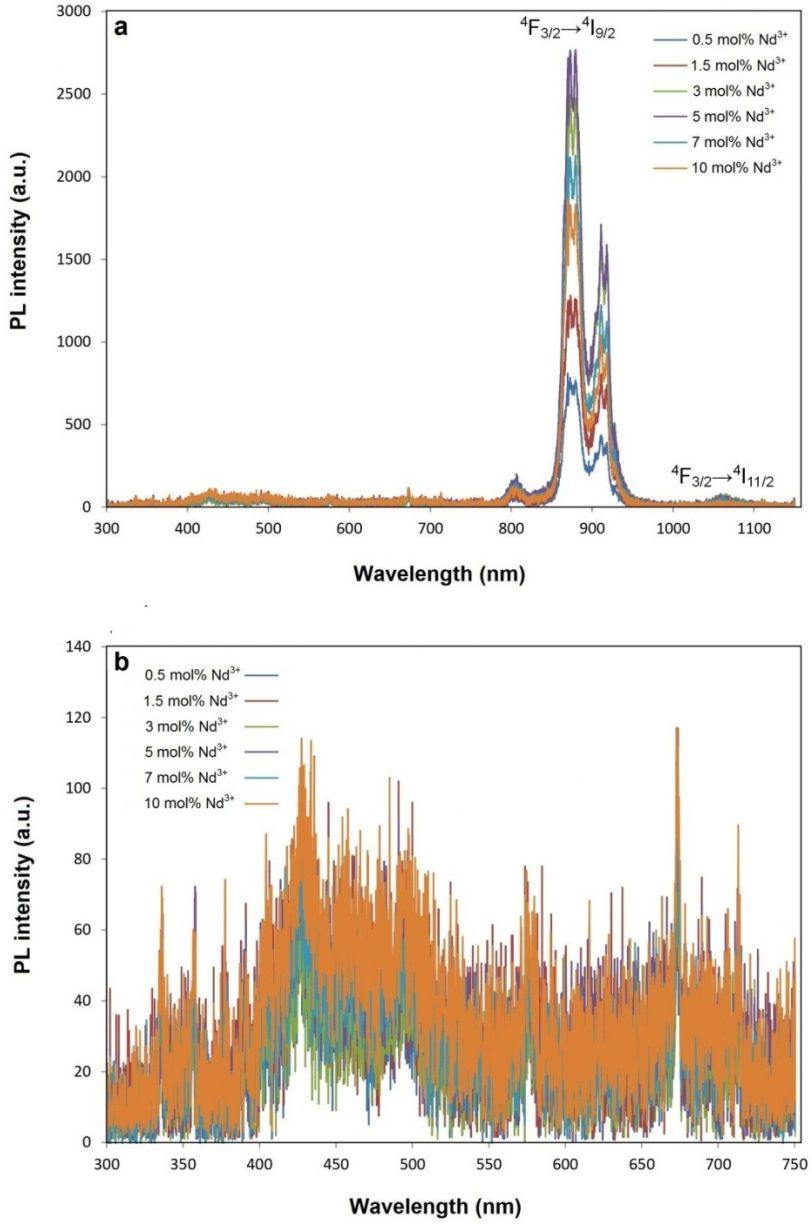

Figure 8: Radioluminescence spectra of the Nd^{3+} doped $PbTa_2O_6$ phosphors, (a) near-infrared emissions, (b) visible emissions.

In Figure 9, the CIE chromaticity diagram of $PbTa_2O_6$:Nd^{3+} under X-ray excitation, and CIE coordinates are given in Table 1. On the basis of the RL spectra, the CIE parameters of all the phosphors were obtained. Usually, the CIE diagram is created using PL emissions, but CIE coordinates can also be presented based on RL spectra as in our previous studies (48, 50). Although there are small coordinate shifts between PL and RL due to the excitation source difference, basically very close values can be obtained. Consequently, the blue region coordinates of Nd^{3+} doped phosphors excited by the strong excitation source or X-ray in the CIE diagram correlate with the visible region transitions corresponding to $^2F(2)_{5/2}\rightarrow{}^4F_{9/2}$, $^2F(2)_{5/2}\rightarrow{}^2H(2)_{11/2}$, $^2F(2)_{5/2}\rightarrow{}^4G_{5/2}$, $^2F(2)_{5/2}\rightarrow{}^4G_{7/2}$ and $^2F(2)_{5/2}\rightarrow{}^4G_{9/2}$.

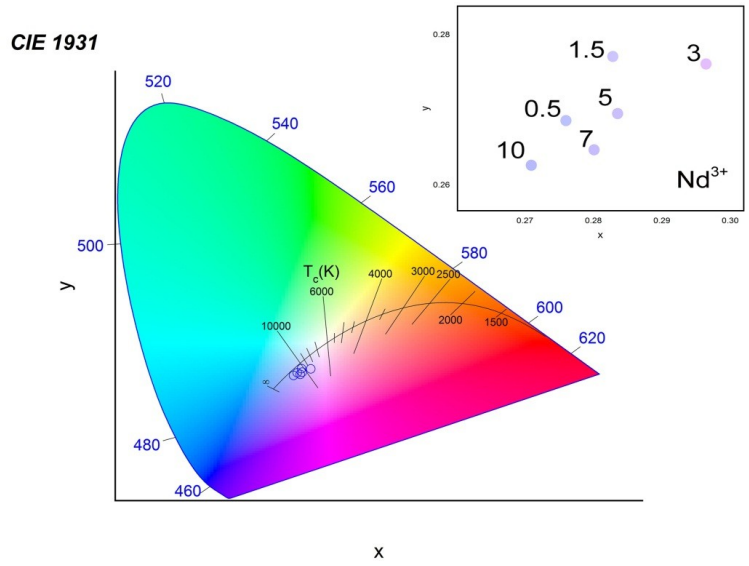

Figure 9: Radioluminescence spectra of the Nd^{3+} doped $PbTa_2O_6$ phosphors, (a) near-infrared emissions, (b) visible emissions.

Table 1: CIE color coordinates of $PbTa_2O_6$:Nd^{3+} phosphors under X-ray excitation source.

Nd^{3+} conc. (%)	CIE coordinates	
	x	***y***
0.5	0.2762	0.2684
1.5	0.2827	0.2769
3	0.2967	0.2763
5	0.2836	0.2696
7	0.2807	0.2649
10	0.2705	0.2627

4. CONCLUSION

The structural and spectral properties of Nd^{3+} doped $PbTa_2O_6$ phosphor fabricated by the conventional solid-state route were investigated in the study. In the XRD results, the single-phase structure Nd^{3+} doped $PbTa_2O_6$ with tetragonal tungsten bronze symmetry were determined between 0.5 and 10 mol % concentrations. SEM micrographs of the grains showed shapeless morphology and the grain sizes varied from 0.5 to 7 μm. EDS results supported some evaporation of Pb during sintering and preservation of the single phase in the structure, similar to the reported studies. The absorption and band gap of $PbTa_2O_6$ host was in agreement with the literature, while the absorptions of Nd^{3+} doped phophors shifted the low band gap energy. The PL emissions in near-infrared region were monitored with the $^4F_{3/2}\rightarrow{}^4I_{9/2}$ and $^4F_{3/2}\rightarrow{}^4I_{11/2}$ transitions at 875 nm, and at 1060 nm of Nd^{3+}, respectively. The RL emissions of $PbTa_2O_6$:Nd^{3+} phosphors were observed by the $^4F_{3/2}\rightarrow{}^4I_{9/2}$, $^4F_{3/2}\rightarrow{}^4I_{11/2}$ transitions in the NIR region, and the weak transitions of the $^2F(2)_{5/2}\rightarrow{}^4F_{9/2}$, $^2F(2)_{5/2}\rightarrow{}^2H(2)_{11/2}$, $^2F(2)_{5/2}\rightarrow{}^4G_{5/2}$, $^2F(2)_{5/2}\rightarrow{}^4G_{7/2}$, $^2F(2)_{5/2}\rightarrow{}^4G_{9/2}$ in the visible region. The strong NIR emissions occurred for the $^4F_{3/2}\rightarrow{}^4I_{9/2}$ transition in both PL and RL, while the the PL and RL emissions decreased over 5 mol% Nd^{3+} due to the concentration quenching. CIE coordinates obtained based on RL emissions were found close to the blue region. The similarity of splitting levels are evident in the PL and RL spectral profiles may be associated with the similarity of the local symmetry of the ligand ions surrounding the Nd^{3+} ion. The Nd^{3+} doped $PbTa_2O_6$ ceramic phosphors with near-infrared luminescence of $^4F_{3/2}\rightarrow{}^4I_{9/2}$ transition may be helpful in future research and photonic applications.

5. CONFLICT OF INTEREST

There is no conflict of interest.

6. REFERENCES

1. Yerpude MM, Nair GB, Dhoble SJ. Green-light emission through energy transfer from Ce^{3+} to Tb^{3+} ions in the $Li2SO_4–Al_2(SO_4)_3$ system. Luminescence 2019;34:382-386. Available from: <DOI>.

2. Yao S, Lv S, Feng Z. Synthesis and photoluminescent properties of Dy^{3+}: $CaYAlO_4$ phosphors. Appl. Phys. A: Mater. Sci. Process. 2021;127:773. Available from: <DOI>.

3. Xue F, Hu Y, Ju G, Chen L, He M, Wang T, Jin Y, Zhang S, Lin J. Photoluminescence and long persistent luminescence properties of a novel green emitting phosphor $Sr_3TaAl_3Si_2O_{14}:Tb^{3+}$. Appl. Phys. A: Mater. Sci. Process. 2016;22:612. Available from: <DOI>.

4. Ekmekçi MK. Influence of europium doping on the crystallization, morphology, and cathodoluminescent properties of $PbNb_2O_6:Eu^{3+}$ phosphors. J. Turk. Chem. Soc. A: Chem. 2022;1129–1140. Available from: <DOI>.

5. Song R, Li H, Zhang H, Tang H, Tang X, Yang J, Zhao H, Zhu J. Tunable luminescence and improved thermostability via Tm–Dy energy transfer in a tellurooxyphosphate phosphor. Appl. Mater. Today 2023;30:101712. Available from: <DOI>.

6. İlhan M, Güleryüz LF. Cathodoluminescence and photoluminescence of $BaTa_2O_6:Sm^{3+}$ phosphor depending on the sintering temperature. Chem. Pap. 2022;76:6963-6974. Available from: <DOI>.

7. Shrivastava R, Khaparde S. Luminescence studies of diopside doped with various concentrations of Dysprosium (III). Res. Chem. Intermed. 2022;48:969-982. Available from: <DOI>.

8. Parganiha M, Dubey V, Shrivastava R, Kaur J. Green light emission in terbium Doped lanthanum zirconate powders. Anal. Chem. Lett. 2022;12:233–243. Available from: <DOI>.

9. Meejitpaisan P, Kaewjaeng S, Ruangthaweep Y, Sangwarantee N, Kaewkhao J. White light emission of gadolinium calcium phosphate oxide and oxyfluoride glasses doped with Dy^{3+}. Mater. Today: Proc. 2021;43:2574–2587. Available from: <DOI>.

10. Luewarasirikul N, Sarachai S, Kim HJ, Kaewkhao J. Enhanced photoluminescence and radioluminescence of Dy^{3+}-doped Ba-Na-B glasses. Radiat. Phys. Chem. 2023;202:110559. Available from: <DOI>.

11. Liu N, Si JY, Cai GM, Tao Y. Crystal structure, luminescence properties and energy transfer of Eu^{3+}/Dy^{3+} doped $GdNbTiO_6$ broad band excited phosphors. RSC Adv. 2016;6:50797. Available from: <DOI>.

12. Li HY, Shen LF, Pun EYB, Lin H. Dy^{3+}-doped germanate glasses for waveguide-typed irradiation light sources. J. Alloys Compd. 2015;646:586-591. Available from: <DOI>.

13. Kavitha V, Rani MP. The influence of Tm^{3+} on the structural, morphological, lifetime, haemocompatibility, and optical properties of sol–gel-synthesized CaS phosphors. Appl. Phys. A: Mater. Sci. Process. 2022;128:1053. Available from: <DOI>.

14. Ding Z, Ding G, Fang L, Peng Z. Luminescent property of $CaWO4:Eu^{3+}$ nanophosphors prepared by molten salt synthesis. Inorg. Nano-Met. Chem. 2022;52:647–652. Available from: <DOI>.

15. İlhan M, Ekmekçi MK, Keskin İÇ. Judd–Ofelt parameters and X-ray irradiation results of $MNb_2O_6:Eu^{3+}$ (M = Sr, Cd, Ni) phosphors synthesized via a molten salt method. RSC Adv. 2021;11:10451. Available from: <DOI>.

16. Gupta SK, Modak B, Tyagi M, Rawat NS, Modak P, Sudarshan K. Harvesting Light from $BaHfO_3/Eu^{3+}$ through ultraviolet, X-ray, and heat stimulation: an optically multifunctional perovskite. ACS Omega 2022:7;5311-5323. Available from: <DOI>.

17. İlhan M, Ekmekçi MK, Demir A, Demirer H. Synthesis and optical properties of novel red–emitting $PbNb_2O_6:Eu^{3+}$ phosphors. J. Fluoresc. 2016;26:1637–1643. Available from: <DOI>.

18. Bruncková H, Medvecký Ľ, Múdra E, Kovalčiková A, Ďurišin J, Šebek M, Girman V. Phase composition of samarium niobate and tantalate thin fims prepared by sol-gel method. Powder Metall. Prog. 2017;17:10–20. Available from: <DOI>.

19. Ekmekçi MK, İlhan M, Güleryüz LF, Mergen A. Study on molten salt synthesis, microstructural determination and white light emitting properties of $CoNb_2O_6:Dy^{3+}$ phosphor. Optik 2017;128:26-33. Available from: <DOI>.

20. He X, Fang B, Zhang S, Lu X, Ding J. Preparation of nanoscale $[(Ba_{0.85}Ca_{0.15})_{0.995}Nd_{0.005}](Ti_{0.9}Hf_{0.1})O_3$ ceramics via hydrothermal method and effect of grain size on multifunctional performance. J. Alloys Compd. 2022;925:166249. Available from: <DOI>.

21. Wang X, Zhao H, Li A, Tian K, Brambilla G, Wang P. Near-infrared luminescence and single-mode laser emission from Nd^{3+} doped compound glass and glass microsphere. Front. Mater. Sci. 2019;6:237. Available from: <DOI>.

22. İlhan M, Keskin İÇ, Çatalgöl Z, Samur R. NIR photoluminescence and radioluminescence characteristics of Nd^{3+} doped $BaTa_2O_6$ phosphor. Int. J. Appl. Ceram. Technol. 2018;15:1594–1601. Available from: <DOI>.

23. Ekmekçi MK, İlhan M, Ege A, Ayvacıklı M. Microstructural and radioluminescence characteristics of Nd^{3+} doped columbite-type $SrNb_2O_6$ phosphor. J. Fluoresc. 2017;27:973–979. Available from: <DOI>.

24. İlhan M, Ekmekçi MK, Oraltay RG, Başak AS. Structural and near-infrared properties of Nd^{3+} activated Lu_3NbO_7 Phosphor. J. Fluoresc. 2017;27:199–203. Available from: <DOI>.

25. Prasad RNA, Vijaya N, Babu P, Mohan NK, Praveena R. Optical absorption and NIR photoluminescence of Nd^{3+}-activated strontium phosphate glasses. J. Electron. Mater. 2020;49:6358-6368. Available from: <DOI>.

26. He X, Fang B, Zhang S, Lu X, Ding J. Preparation and properties of Nd-doped BCTH lead-free ceramics by solid-phase twin crystal method. Curr. Appl. Phys. 2022;38:30-39. Available from: <DOI>.

27. Golyeva EV, Vaishlia EI, Kurochkin MA, Kolesnikov EY, Lähderanta E, Semencha AV, Kolesnikov IE. Nd^{3+} concentration effect on luminescent properties of $MgAl2O_4$ nanopowders synthesized by modified Pechini method. J. Solid State Chem. 2020:289;121486. Available from: <DOI>.

28. Ekmekçi MK, Erdem M, Başak AS, İlhan M, Mergen A. Molten salt synthesis and optical properties of Eu^{3+}, Dy^{3+} or Nd^{3+} doped $NiNb_2O_6$ columbite-type phosphors. Ceram. Int. 2015;41:9680–9685. Available from: <DOI>.

29. Mahamuda Sk, Swapna K, Rao AS, Jayasimhadri M, Sasikala T, Pavani K, Moorthy LR. Spectroscopic properties and luminescence behavior of Nd^{3+} doped zinc alumino bismuth borate glasses. J. Phys. Chem. 2013;74;1308–1315. Available from: <DOI>.

30. İlhan M, Katı Mİ, Keskin İÇ, Güleryüz LF. Evaluation of structural and spectroscopic results of tetragonal tungsten bronze $MTa_2O_6:Eu^{3+}$ (M = Sr, Ba, Pb) phosphors and comparison on the basis of Judd-Ofelt parameters. J. Alloy. Comp. 2022;901:163626. Available from: <DOI>.

31. İlhan M, Güleryüz LF, Keskin İÇ, Katı Mİ. A comparison of spectroscopic properties of Dy^{3+}-doped tetragonal tungsten bronze MTa_2O_6 (M = Sr, Ba, Pb) phosphors based on Judd–Ofelt parameters. Mater. Sci: Mater. Electron 2022;33:16606–16620. Available from: <DOI>.

32. İlhan M, Keskin İÇ, Gültekin S. Assessing of photoluminescence and thermoluminescence properties of Dy^{3+} doped white light emitter TTB-lead metatantalate phosphor. J. Electron. Mater. 2020;49:2436-2449. Available from: <DOI>.

33. Nakauchi D, Okada G, Koshimizu M, Yanagida T. Optical and scintillation properties of Nd-doped $SrAl_2O_4$ crystals. J. Rare Earths 2016;34:757–762. Available from: <DOI>.

34. Kamada K, Kurosawa S, Yamaji A, Shoji Y, Pejchal J, Ohashi Y, Yokota Y, Yoshikawa A. Growth of Nd doped $(Lu, Gd)_3(Ga, Al)_5O_{12}$ single crystal by the micro pulling down method and their scintillation properties. Opt. Mater. 2015;41:32-35. Available from: <DOI>.

35. Sugiyama M, Fujimoto Y, Yanagida T, Yamaji A, Yokota Y, Yoshikawa A. Growth and scintillation properties of Nd-doped $Lu_3Al_5O_{12}$ single crystals by Czochralski and micro-pulling-down methods. J. Cryst. Growth 2013;362:178–181. Available from: <DOI>.

36. Yanagida T, Fujimoto Y, Ishizu S, Fukuda K. Spectrochim. Optical and scintillation properties of Nd differently doped $YLiF_4$ from VUV to NIR wavelengths. Opt. Mater. 2015;41:36–40. Available from: <DOI>.

37. Francombe MH, Lewis B. Structural, dielectric and optical properties of ferroelectric lead metaniobate. Acta Cryst. 1958;11:696. Available from: <DOI>.

38. Subbarao EC, Shirane G, Jona F. X-ray, dielectric, and optical study of ferroelectric lead metatantalate and related compounds. Acta Cryst. 1960;13:226. Available from: <DOI>.

39. Simon A, Jean R. Solid-state chemistry and non-linear properties of tetragonal tungsten bronzes materials. C. R. Chim. 2006;9:1268–1276. Available from: <DOI>.

40. İlhan M. Synthesis, structural characterization, and photoluminescence properties of TTB-type $PbTa_2O_6:Eu^{3+}$ phosphor. Int. J. Appl. Ceram. Technol. 2017;14:1144–1150. Available from: <DOI>.

41. İlhan M, Keskin İÇ. Evaluation of structural behaviour, radioluminescence, Judd-Ofelt analysis and thermoluminescence kinetic parameters of Eu^{3+} doped TTB–type lead metaniobate phosphor. Phys. B: Condens. Matter 2020;585:412106. Available from: <DOI>.

42. Wang BX, Krogstad MJ, Zheng H, Osborn R, Rosenkranz S, Phelan D. Active and passive defects in tetragonal tungsten bronze relaxor ferroelectrics. J. Phys. Condens. Matter 2022;34:405401. Available from: <DOI>.

43. Kato H, Kudo A. New tantalate photocatalysts for water decomposition into H_2 and O_2. Chem. Phys. Lett. 1998;487:492. Available from: <DOI>.

44. Zhang W, Kumada N, Takei T, Yamanaka J, Kinomura N. Preparation and crystal structure of H-$BaTa_2O_6$-type $K_{1.83}Ba_{4.17}Nb_{12.18}O_{36}$ and dielectric properties of the related compounds. Mater. Res. Bull. 2005;40:1177−1186. Available from: <DOI>.

45. Li G, Cheng L, Liao F, Tian S, Jing X, Lin J. Luminescent and structural properties of the series $Ba_{6-x}Eu_xTi_{2+x}Ta_{8-x}O_{30}$ and $Ba_{4-y}K_yEu_2Ti_{4-y}Ta_{6+y}O_{30}$. J. Solid State Chem. 2004;177:875–882. Available from: <DOI>.

46. Tauc J. Optical properties and electronic structure of amorphous Ge and Si. Mater. Res. Bull. 1968;3(1):37-46. Available from: <DOI>.

47. Boltersdorf J, Wong T, Maggard PA. Synthesis and optical properties of Ag(I), Pb(II), and Bi(III) tantalate-based photocatalysts. ACS Catal. 2013;3:2943–2953. Available from: <DOI>.

48. Keskin İÇ, Türemiş M, Katı Mİ, Gültekin S, Arslanlar YT, Çetin A, Kibar R. Detailed luminescence (RL, PL, CL, TL) behaviors of Tb^{3+} and Dy^{3+} doped $LiMgPO_4$ synthesized by sol-gel method. J. Lumin. 2020;225:117276. <DOI>.

49. Ahmed AS, Muhamed SM, Singla ML, Tabassum S, Naqvi AH, Azam A. Band gap narrowing and fluorescence properties of nickel doped SnO_2 nanoparticles. J. Lumin. 2011;131:1–6. Available from: <DOI>.

50. Keskin İÇ. Radioluminescence results, thermoluminescence analysis and kinetic parameters of $Y_2O_3:Ln^{3+}$ (Ln: Dy, Nd, Sm) nanophosphors obtained by sol-gel method. Ceram. Int. 2022;48(14):20579–20590. Available from: <DOI>.

51. Burstein E. Anomalous Optical Absorption Limit in InSb. Phys. Rev. 1954;93:632. <DOI>.

52. Blasse G. Energy transfer between inequivalent Eu^{2+} ions. J. Solid State Chem. 1986;62:207–211. Available from: <DOI>.

53. Blasse G. Energy transfer in oxidic phosphors. Philips Res. Rep. 1969;24:131. Available from: <DOI>.

54. Ayvacıkli M, Kotan Z, Ekdal E, Karabulut Y, Canimoglu A, Guinea JG, Khatab A, Henini M, Can N. Solid state synthesis of $SrAl_2O_4:Mn^{2+}$ co-doped with Nd^{3+} phosphor and its optical properties. J. Lumin. 2013;144:128–132. Available from: <DOI>.